J. Fluid Mech. (2010), *vol.* 642, *pp.* 421–443.
doi:10.1017/S0022112009991911

Shock-resolved Navier–Stokes simulation of the Richtmyer–Meshkov instability start-up at a light–heavy interface

R. M. J. KRAMER[1]†, D. I. PULLIN[1], D. I. MEIRON[2] AND C. PANTANO[3]

[1]Graduate Aeronautical Laboratories, California Institute of Technology, MC 205-45, Pasadena, CA 91125, USA

[2]Applied and Computational Mathematics, California Institute of Technology, MC 205-45, Pasadena, CA 91125, USA

[3]Department of Mechanical Science and Engineering, University of Illinois at Urbana-Champaign, Urbana, IL 61801, USA

(Received 22 April 2009; revised 28 August 2009; accepted 29 August 2009; first published online 9 December 2009)

The single-mode Richtmyer–Meshkov instability is investigated using a first-order perturbation of the two-dimensional Navier–Stokes equations about a one-dimensional unsteady shock-resolved base flow. A feature-tracking local refinement scheme is used to fully resolve the viscous internal structure of the shock. This method captures perturbations on the shocks and their influence on the interface growth throughout the simulation, to accurately examine the start-up and early linear growth phases of the instability. Results are compared to analytic models of the instability, showing some agreement with predicted asymptotic growth rates towards the inviscid limit, but significant discrepancies are noted in the transient growth phase. Viscous effects are found to be inadequately predicted by existing models.

Key words: computational methods, nonlinear, shock waves

1. Introduction

The Richtmyer–Meshkov (RM) instability, named for the foundational work on this problem by Richtmyer (1960) and Meshkov (1969), occurs when a shock collides with a perturbed interface between fluids of different density. The problem is shown schematically in figure 1 for the planar reflected-shock case, where it is assumed that the incident shock travels from the light fluid into the heavy fluid ($\rho_{0'} > \rho_0$) in a two-dimensional Cartesian geometry.

The initial growth of the interface perturbation is driven by vorticity deposited at the interface by baroclinic torque, a result of the misalignment of the pressure gradient across the shock with the density gradient across the interface. The focus of this work will be on the early-time evolution of the RM instability, which exhibits damped oscillation in the growth rate (Yang, Zhang & Sharp 1994; Wouchuk 2001; Herrmann, Moin & Abarzhi 2008), as a result of acoustic waves trapped between the reflected and transmitted shocks and the vorticity field behind the decaying shock front perturbations. At later times, the perturbation grows larger, distorting the interface and leading to formation of 'bubbles' and 'spikes' that excite secondary instabilities

† Email address for correspondence: rmjkramer@gmail.com

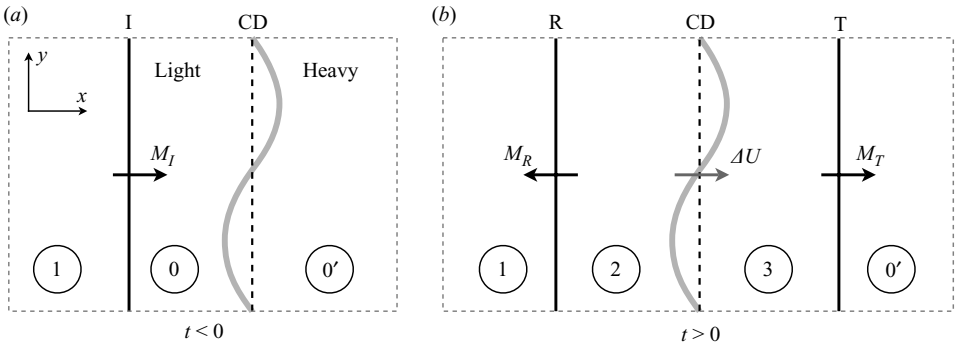

FIGURE 1. Schematic of the reflected shock RM problem, before (*a*) and after (*b*) interaction of the incident shock with the interface at $t=0$. Fluid states are labelled 0′ and 0 through 3.

and eventually result in chaotic mixing of the light and heavy fluids (Zhang & Sohn 1997; Collins & Jacobs 2002; Hill, Pantano & Pullin 2006; Herrmann *et al.* 2008).

The simplest model of the RM instability is the impulsive model of Richtmyer (1960). This models the shock impact on the contact discontinuity as an impulsive acceleration of a sinusoidally perturbed interface of zero thickness between two inviscid incompressible fluids. For small-amplitude perturbations, this predicts a linear growth rate in time for the interface amplitude, which was validated by Richtmyer's own simulations. This has been shown to agree at least qualitatively with experimental investigations of the instability, first by Meshkov (1969) and by many authors subsequently for weak shocks (see e.g. Brouillette & Sturtevant 1994; Jones & Jacobs 1997; Collins & Jacobs 2002), where the linear growth rate is achieved in an asymptotic sense. For stronger shocks, however, the assumptions of the impulsive model break down and the growth rate is no longer accurately predicted (Yang *et al.* 1994).

More advanced models of the instability fall generally into one of two categories. The first covers analytic improvements to the simple impulsive model, where its various assumptions are generalized to improve the growth rate prediction under certain conditions. Those considered in this study include the effect of a distributed initial interface (Saffman & Meiron 1989; Mikaelian 1991; Brouillette & Sturtevant 1994), viscosity (Mikaelian 1993; and in more advanced form, Carlès & Popinet 2001) and finite proximity of the reflected and transmitted shocks (Lombardini 2008).

Models in the second category are based on linearization of the Euler equations about the one-dimensional Riemann solution of the shock-interface problem in the small-amplitude approximation. These obtain estimates for the asymptotic growth rate either (semi-) analytically by series expansion (Wouchuk & Nishihara 1997 and Wouchuk 2001 are considered here) or by numerical solution (Yang *et al.* 1994). It is this latter approach that leads into the method used for the simulations presented in this work.

A fundamental challenge encountered with simulation of the RM instability is the numerical treatment of the shocks in the domain. Since the shock thickness is of the order of the gas mean free path length, which is two to three orders of magnitude smaller than the next smallest scale in the simulation, full resolution of the shock structure has, until now, been impossible. Furthermore, because of the weak influence of viscosity in most problems of interest, an inviscid fluid assumption is often made. In both cases, shock capturing or tracking methods are generally used (e.g. Hill *et al.* 2006; Herrmann *et al.* 2008) and so potentially suffer first-order error at the shock (Engquist & Sjögreen 1998).

Examples of high-order simulation of the RM instability are limited, in part for this reason. The recent work of Yee & Sjögreen (2007) uses a shock-capturing sixth-order filter method in their Navier–Stokes (NS) simulation, and as far as the authors are aware, no attempt has been made to resolve the full NS shock structure in the context of an RM simulation until this work. Resolution of the shock and thin contact region is achieved here by multiple levels of local refinement using the stable high-order grid-interface closures developed in Kramer, Pantano & Pullin (2007).

This high-fidelity simulation permits a detailed investigation of the start-up and linear growth phases of the instability. The distributed interaction of the shock and interface is observed and perturbations developed by the shocks are tracked throughout the simulation. These features, along with physical viscous effects, are found to result in transient growth effects not predicted or observed by existing inviscid models and simulations.

2. Linearized Navier–Stokes equations

In this investigation of the RM instability, the two-dimensional NS equations are linearized about a fully resolved numerical solution for the base flow, in a frame of reference in which the interface is stationary for $t < 0$. Shocks and the interface are treated as continuous features, and it is assumed that the perturbation amplitude remains small throughout the simulation. The problem is also simplified by considering a single fluid, such that $\gamma_0 = \gamma_{0'} = \gamma$. The time origin $t = 0$ is defined as the time at which the shock reaches the interface in the inviscid Riemann problem for the base flow.

Starting with the general compressible NS equations for a Newtonian fluid with zero bulk viscosity and Fourier heat conduction, two-dimensional Cartesian axes (x, y) are defined such that the shocks propagate initially in the direction parallel to the x-axis. It is further assumed that viscosity and conductivity are constant, an acceptable approximation for weak shocks where the change in temperature is small. In the strongest shock case considered in this work, $M_I = 2.20$, the constant-viscosity assumption results in a velocity profile that is within 10 % of the varying viscosity solution.

For the equation of state, a perfect gas is specified such that

$$p = \rho R T, \tag{2.1}$$

$$e = C_V T = \frac{1}{\gamma - 1}\frac{p}{\rho}. \tag{2.2}$$

A non-dimensionalization is defined in terms of reference parameters ρ_0 and p_0 at state 0, using the incident shock velocity U_I for the velocity scale. A global length scale is provided by the mean free path in state 0, ℓ_0, given by

$$\ell_0 = \nu_0 \frac{8}{5}\sqrt{\frac{2}{\pi R T_0}}, \tag{2.3}$$

where ν_0 is the kinematic viscosity of the fluid in state 0. This is clearly a viscous length scale. For state 0 having standard atmospheric conditions listed in table 1, the mean free path length is $\ell_0 = 6.65 \times 10^{-8}$ m, with a corresponding global time scale ℓ_0/U_I of $O(10^{-10})$ s. In the post-shock regime, a characteristic sound speed $\tilde{a}$ may be defined in terms of an averaged kinematic viscosity $\nu = (\mu_2 + \mu_3)/(\rho_2 + \rho_3)$ as

$$\tilde{a} \equiv \frac{\nu}{\ell_0} = \frac{\mu_2 + \mu_3}{\rho_2 + \rho_3}\frac{1}{\ell_0}. \tag{2.4}$$

γ	1.4		
ρ_0 (kg m^{-3})	1.205		
p_0 (kPa)	101.3		
ℓ_0 (m)	6.65×10^{-8}		
M_I	1.05	1.21	2.20
U_I (m s^{-1})	360.2	415.1	754.7
Δ_I (m)	3.29×10^{-6}	7.82×10^{-7}	1.37×10^{-7}
ℓ_0/U_I (s)	1.85×10^{-10}	1.60×10^{-10}	8.81×10^{-11}

TABLE 1. Dimensional parameters and scalings for each Mach number case considered. Non-dimensional variables are normalized by the length scale ℓ_0 and time scale ℓ_0/U_I.

This will be used to define a Reynolds number for the instability in § 5.1. For expediency, from this point onward throughout this work, all variables refer to non-dimensional values without change in notation, unless otherwise indicated.

The solution to the NS equations for a small single-mode sinusoidal perturbation in the y direction of a one-dimensional base flow is presumed to take the form

$$u = \bar{u}(x,t) + \epsilon u'(x,t)\mathrm{e}^{\mathrm{i}ky}, \tag{2.5}$$

$$v = \epsilon v'(x,t)\mathrm{e}^{\mathrm{i}ky}, \tag{2.6}$$

$$\rho = \bar{\rho}(x,t) + \epsilon \rho'(x,t)\mathrm{e}^{\mathrm{i}ky}, \tag{2.7}$$

$$p = \bar{p}(x,t) + \epsilon p'(x,t)\mathrm{e}^{\mathrm{i}ky}, \tag{2.8}$$

where the small parameter $\epsilon \ll 1$, the overbar indicates the base flow variables that are one-dimensional but generally unsteady, and prime quantities denote the first-order perturbation variables. The wavenumber k is generally complex and normalized by the scale $1/\ell_0$. This approach differs from standard stability analysis in that the base flow depends on time according to the viscous nonlinear shock-resolved dynamics. Substituting (2.5)–(2.8) into the general nonlinear equations and expanding in powers of ϵ, at order ϵ^0 the base flow equations are obtained:

$$\frac{\partial \bar{\rho}}{\partial t} = -\frac{\partial(\bar{\rho}\bar{u})}{\partial x}, \tag{2.9}$$

$$\frac{\partial(\bar{\rho}\bar{u})}{\partial t} = -\frac{\partial}{\partial x}\left(\frac{\bar{p}}{\gamma M_I^2} + \bar{\rho}\bar{u}^2 - \frac{4}{3}\frac{1}{Re}\frac{\partial \bar{u}}{\partial x}\right), \tag{2.10}$$

$$\frac{\partial}{\partial t}\left(\frac{\bar{p}}{\gamma M_I^2} + \beta\bar{\rho}\bar{u}^2\right) = -\frac{\partial}{\partial x}\left(\frac{\bar{p}\bar{u}}{M_I^2} + \beta\bar{\rho}\bar{u}^3 - \frac{1}{Pr\,Re\,M_I^2}\frac{\partial \bar{T}}{\partial x} - \frac{4}{3}\frac{\gamma-1}{Re}\bar{u}\frac{\partial \bar{u}}{\partial x}\right), \tag{2.11}$$

where $\beta = (\gamma - 1)/2$. These are the familiar (nonlinear) one-dimensional compressible NS equations. At order ϵ, the following system is derived:

$$\frac{\partial \rho'}{\partial t} = -\frac{\partial}{\partial x}[\bar{\rho}u' + \rho'\bar{u}] - \mathrm{i}k\bar{\rho}v', \tag{2.12}$$

$$\frac{\partial}{\partial t}\left(\bar{\rho}u' + \rho'\bar{u}\right) = -\frac{\partial}{\partial x}\left[\frac{p'}{\gamma M_I^2} + \rho'\bar{u}^2 + 2\bar{\rho}\bar{u}u' - \frac{1}{Re}\left(\frac{4}{3}\frac{\partial u'}{\partial x} + \frac{1}{3}\mathrm{i}kv'\right)\right] - \mathrm{i}k\bar{\rho}\bar{u}v' - \frac{1}{Re}k^2u', \tag{2.13}$$

$$\frac{\partial}{\partial t}\left(\bar{\rho}v'\right) = -\frac{\partial}{\partial x}\left[\bar{\rho}\bar{u}v' - \frac{1}{Re}\left(\frac{\partial v'}{\partial x} + \frac{1}{3}\mathrm{i}ku'\right)\right] - \mathrm{i}k\frac{p'}{\gamma M_I^2} - \frac{1}{Re}\frac{4}{3}k^2v', \tag{2.14}$$

$$\begin{aligned}\frac{\partial}{\partial t}&\left(\frac{p'}{\gamma M_I^2} + \beta(\rho'\bar{u}^2 + 2\bar{\rho}\bar{u}u')\right)\\ &= -\frac{\partial}{\partial x}\left[\frac{p'\bar{u} + \bar{p}u'}{M_I^2} + \beta(\rho'\bar{u}^3 + 3\bar{\rho}\bar{u}^2u') - \frac{1}{PrReM_I^2}\frac{\partial T'}{\partial x} - \frac{4}{3}\frac{\gamma-1}{Re}\left(\bar{u}\frac{\partial u'}{\partial x} + u'\frac{\partial \bar{u}}{\partial x}\right)\right]\\ &\quad - \mathrm{i}kv'\left(\frac{\bar{p}}{M_I^2} + \beta\bar{\rho}\bar{u}^2\right) - \frac{1}{PrRe}k^2\frac{T'}{M_I^2} + \frac{\gamma-1}{Re}\bar{u}\left(\frac{1}{3}\mathrm{i}k\frac{\partial v'}{\partial x} - k^2u'\right).\end{aligned} \tag{2.15}$$

Equations (2.12)–(2.15) for the first-order perturbations form a linear system of partial differential equations with variable coefficients (that are the base flow solution).

This system depends on four parameters: the incident shock Mach number M_I, γ and the Reynolds and Prandtl numbers, Re and Pr. For consistency with the analytic NS shock solution used for the initial condition, the Reynolds number for these equations is based on the molecular viscosity derived from kinetic theory, such that

$$Re = \frac{\sqrt{\gamma M_I^2}}{k_2}, \quad \text{where} \quad k_2 = \frac{5}{8}\sqrt{\frac{\pi}{2}}.$$

Similarly, for the Prandtl number, $Pr = 3/4$ is required (Whitham 1974). Note that for a real wavenumber k, provided that the initial perturbed fields ρ', u' and p' are real and v' has zero real part, the solution to (2.9)–(2.15) will evolve to have v' purely imaginary, and all other fields purely real.

The inviscid version of the base flow describes a Riemann problem, which may be solved analytically to obtain speeds and locations for the shocks and interface in the inviscid limit. Solutions to the Riemann problem for the parameter values chosen for simulation are shown in table 2. The pre-shock Atwood number A and post-shock Atwood number A^+ are defined in terms of the density solution by

$$A = \frac{\rho_{0'} - \rho_0}{\rho_{0'} + \rho_0} \quad \text{and} \quad A^+ = \frac{\rho_3 - \rho_2}{\rho_3 + \rho_2}.$$

In all cases, both light (hot) and heavy (cold) gases are air where state 0 (the reference state) is at standard atmospheric conditions having density $\rho_0 = 1.205\,\mathrm{kg\,m^{-3}}$ and pressure $p_0 = p_{0'} = 101.3$ kPa. Velocities are normalized relative to the incident shock velocity U_I.

3. Numerical method

For simulation of the linearized RM instability, the strategy is to solve the base flow equations (2.9)–(2.11) and the first-order perturbation equations (2.12)–(2.15) simultaneously. The numerical solution obtained for (2.9)–(2.11) is the unsteady one-dimensional base flow, corresponding to the viscous version of the shock-interface interaction problem. The solution to (2.12)–(2.15) proceeds using the (x, t)-dependent coefficients from the base flow, and describes the first-order perturbation of the RM instability.

The basic numerical method uses a fourth-order explicit finite-difference scheme to approximate the spatial derivatives, with local refinement (described in § 3.3) using the one-dimensional grid interface schemes from Kramer *et al.* (2007). Interpolation to advance or create refined region(s) of the grid between time steps uses the sixth-order

M_I	1.05	1.05	1.21	1.21	2.20	2.20
A	0.2	0.6	0.2	0.6	0.2	0.6
M_T	1.0552	1.0672	1.2333	1.2884	2.3570	2.7493
U_T	0.8205	0.5082	0.8322	0.5324	0.8748	0.6248
M_R	1.0049	1.0161	1.0183	1.0616	1.0633	1.2232
U_R	−0.8951	−0.9060	−0.6321	−0.6703	0.002562	−0.09645
u_1	0.07748	0.07748	0.2642	0.2642	0.6612	0.6612
ρ_1	1.0840	1.0840	1.3590	1.3590	2.9512	2.9512
p_1	1.1196	1.1196	1.5415	1.5415	5.4800	5.4800
ΔU	0.06965	0.05166	0.2376	0.1764	0.5978	0.4518
ρ_2	1.0928	1.1132	1.4005	1.4999	3.2655	4.0781
p_2	1.1323	1.1621	1.6079	1.7699	6.3149	8.6517
ρ_3	1.63914	4.4526	2.0992	5.9818	4.7369	14.445
A^+	0.19999	0.59998	0.1996	0.5991	0.1839	0.5597
$\tilde{a}$	0.4616	0.3127	0.0752	0.2266	0.1463	0.0325

TABLE 2. Riemann solutions for the parameter sets used in the simulations of the RM instability. Values shown are normalized by ρ_0, p_0 and U_I, as appropriate, using the values from table 1. Subscripts correspond to the states shown in figure 1. The parameter $\tilde{a}$ is defined by (2.4) and is shown normalized by U_I.

scheme of Fornberg (1988), a higher order method than the finite-difference scheme that minimizes the truncation error at newly refined regions. Second derivatives are evaluated by applying the first derivative scheme twice. Time integration uses the third-order Runge–Kutta (RK32) scheme from Butcher (2003), with uniform time stepping. This approach can be shown to be numerically stable and contribute no numerical dissipation (Kramer *et al.* 2007). The lack of artificial dissipation in the numerical method ensures that only physical viscous effects are observed in the simulation results. Convergence of the method is also demonstrated (see § 3.4).

3.1. *Boundary conditions*

Characteristic boundary conditions are implemented using the simultaneous approximation term (SAT) method of Carpenter, Gottlieb & Abarbanel (1994). The method for the one-dimensional base-flow equations follows closely that proposed by Svärd, Carpenter & Nordström (2007) for the NS equations. For the two-dimensional first-order equations, because these are linear (though with non-constant coefficients) and have the same characteristics as the base flow, the implementation of characteristic boundary conditions is straightforward. Additional boundary conditions for the NS equations are given by zero-gradient conditions on temperature (upstream) and velocity (downstream) for both fields. Full details of the method are given in Kramer (2009).

For all time, the boundary state at the left (upstream) end is state 1, and at the right (downstream) end, state 0′. The computational domain is chosen to be large enough to contain the reflected and transmitted shocks (including tails) until the end of the simulation. Note that both boundary states are constant throughout the simulation.

3.2. *Initial condition*

A discontinuous density interface with a sinusoidal perturbation, given in terms of an initial amplitude h_0 by

$$\rho(x, y, t = 0) = \begin{cases} \rho_0, & x < h_0 \sin(ky), \\ \rho_{0'}, & x > h_0 \sin(ky), \end{cases} \tag{3.1}$$

where the interface is centred at $x = 0$, is unstable in this numerical implementation, as the step-function discontinuity introduces Gibbs-type oscillation that cannot be dissipated by the numerical method and grows with time. The alternative is to model the contact surface more realistically with a diffuse density interface, using the solution from Duff, Harlow & Hirt (1962),

$$\rho(x, y, t = 0) = \frac{\rho_{0'} + \rho_0}{2} + \frac{\rho_{0'} - \rho_0}{2} \operatorname{erf}(x + h_0 \mathrm{e}^{\mathrm{i}ky}). \tag{3.2}$$

Closely related is the alternative profile

$$\rho(x, y, t = 0) = \frac{\rho_{0'} + \rho_0}{2} + \frac{\rho_{0'} - \rho_0}{2} \tanh(x + h_0 \mathrm{e}^{\mathrm{i}ky}), \tag{3.3}$$

which is easier to analyse, and under the appropriate scaling, differs from the error function profile by less than 3.5 % (Mikaelian 1991). Comparison of solutions initialized with each initial profile also show that this choice has little influence on the post-shock-interface shape or position (Kramer 2009).

For the problem described by (2.9)–(2.15), the perturbed interface given in (3.3) is approximated within the constraints of the form of the linearization, $\bar{\rho} + \epsilon\rho'(x, t)\mathrm{e}^{\mathrm{i}ky}$. Generalizing the profile for a thickness Δ_C, the Taylor expansion of (3.3) about x for small-amplitude h_0 yields the initial condition

$$\bar{\rho}(x, t = 0) = \frac{\rho_{0'} + \rho_0}{2} + \frac{\rho_{0'} - \rho_0}{2} \tanh(2x/\Delta_C), \tag{3.4}$$

$$\epsilon\rho'(x, t = 0) = \frac{\rho_{0'} - \rho_0}{2} \frac{2h_0}{\Delta_C} \operatorname{sech}^2(2x/\Delta_C), \tag{3.5}$$

where for consistency with the linearization assumption (2.7), we require $\epsilon = h_0/\Delta_C \ll 1$. All other fields are initialized to be constant across the interface region.

The incident shock is initialized using the constant-viscosity NS shock solution for the given incident Mach number M_I, based on the implementation in Kramer *et al.* (2007) of the solution from Whitham (1974). The domain upstream of the shock, state 1, is uniform and initialized to the Rankine–Hugoniot conditions based on the incident shock strength. In the remainder of the computational domain, downstream of the interface and shock, the initial condition is the quiescent state $0'$.

3.3. *Refinement tracking*

Local refinement of the computational domain is used in the vicinity of the shocks and the interface to efficiently resolve the full solution. Because one or more flow features are necessarily in motion relative to the solution reference frame, the local refinement scheme for the RM problem must be designed to track each feature of interest with time, i.e. an adaptive mesh refinement (AMR) scheme is necessary. In the general case, AMR requires complicated solution gradient detection algorithms to ensure that adequate refinement occurs where it is needed. For the RM problem, however, a simpler approach may be adopted, using the one-dimensional Riemann solution to give an *a priori* indication of where refinement of the solution will be required. Thus the inviscid Euler solution may be used to design a refinement scheme that tracks the solution features of interest, with a relatively simple algorithm that shifts the refinement regions based on the known locations of the shocks and interface. This is demonstrated by figure 2, which shows the refinement scheme in (x, t) space, overlaying the x–t diagram of the Riemann solution.

Two levels of refinement are used at the transmitted shock and the interface, each of factor two with respect to the previous level, for an overall refinement of a factor of 4. A single refinement level was usually sufficient to resolve the much weaker

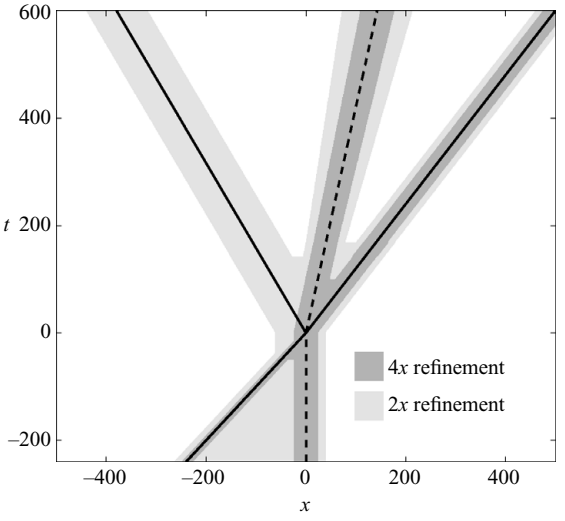

FIGURE 2. A two-level grid refinement scheme for $M_I = 1.21$ and $A = 0.2$, overlaying the x–t diagram for this problem. The shaded areas show how the refined regions follow the flow features based on the Riemann solution; the darker regions indicates a second level of refinement.

reflected shock. Grid movement occurs at a rate specified by the speed of each feature as determined from the inviscid Riemann solution. To preserve the integrity of the grid, a shift is performed only once the feature has travelled a distance equivalent to at least one coarse cell, so the refinement advances in appropriate multiples of the coarse grid spacing. Additionally, to ensure that the interface perturbation remains properly resolved, the refinement region gradually extends while it convects to follow the slow diffusion of the interface.

In the case of $M_I = 2.20$ and $A = 0.6$, an additional level of refinement was required to resolve a very steep gradient that appears during interaction of the incident shock with the interface. Otherwise, this sharp peak resulted in non-physical oscillation at the trailing corner of the transmitted shock for the remainder of the simulation. With a small region of additional refinement at the transmitted shock, this oscillation disappeared and the solution remained smooth for all time.

3.4. *Verification*

Verification of the discrete implementation of the two-dimensional system (2.9)–(2.15) was performed using the method of manufactured solutions to provide reference solutions for the numerical method. Details of this study are given in Kramer (2009). For the RM problem, convergence was tested by performing a sequence of uniform-grid simulations for the case of $M_I = 2.20$ and $A = 0.2$. Because no analytic solution exists to this problem, comparison is made to a more refined numerical solution of resolution $\Delta x = 1/16$.

Table 3 shows that the expected fourth-order convergence rate is achieved asymptotically as the grid is refined, for both base and perturbed solutions. For the coarsest grids, the transmitted shock is under-resolved, which causes non-physical oscillation at its trailing edge and is detrimental to the convergence rate. Oscillation in the transmitted shock was generally found to be a good indicator of sufficient

	Error based on $\bar{\rho}$				Error based on ρ'			
Δx	$\log_{10}(L_2)$	Rate	$\log_{10}(L_\infty)$	Rate	$\log_{10}(L_2)$	Rate	$\log_{10}(L_\infty)$	Rate
1/2	−0.667		−0.730		−1.965		−2.083	
1/4	−1.527	2.86	−1.378	2.15	−2.588	2.07	−2.507	1.41
1/8	−2.614	3.61	−2.350	3.23	−3.578	3.29	−3.324	2.71
1/12	−3.424	4.60	−3.143	4.50	−4.365	4.47	−4.086	4.33

TABLE 3. Convergence performance of the uniform-grid RM simulation, compared to the reference numerical solution on a grid of $\Delta x = 1/16$, for both L_2 (average) and L_∞ (uniform) norms.

resolution. Detailed testing of the local refinement scheme is described in Kramer *et al.* (2007).

3.5. *Amplitude measurement*

The fundamental quantity of interest for investigation of the RM instability is the amplitude of the perturbation on the density interface $h(t)$ defined most generally as

$$h(t) = \frac{1}{2}|x_{C,peak} - x_{C,trough}|, \tag{3.6}$$

where $x_C(y, t)$ is the centreline of the interface perturbation (Lombardini 2008). In the linearized theory, the amplitude is recovered directly from the definition $x_C = -h(t)\mathrm{e}^{\mathrm{i}ky}$. For the present distributed case, defining the normalized density function ψ,

$$\psi(x, y, t) = \frac{\rho(x, y, t) - \rho_a}{\rho_b - \rho_a}, \tag{3.7}$$

having the linearized form

$$\psi(x, y, t) \approx \bar{\psi}(x, t) - \psi'(x, t)\mathrm{e}^{\mathrm{i}ky}, \tag{3.8}$$

where the reference densities ρ_a and ρ_b are chosen such that $\bar{\psi} \in [0, 1]$, the interface amplitude $h(t)$ is given by the integral definition

$$h(t) = \int_{-x_l}^{x_r} \psi' \mathrm{d}x. \tag{3.9}$$

The limits $[-x_l, x_r]$ are chosen such that the interface perturbation is wholly contained within the window of integration and the neighbouring shock perturbations are avoided. Simple algebra will show that this definition recovers the appropriate perturbation amplitude for both distributed and discontinuous interfaces (Kramer 2009).

The definition of amplitude by (3.9) causes some difficulty near $t = 0$, during interaction of the shock with the interface, when the interface becomes indistinguishable from the shock(s). This is illustrated in figure 3. Shock-interface interaction in the viscous problem is a distributed process, beginning when the head of the incident shock reaches the tail of the interface, and continuing until the tails of both reflected and transmitted shocks separate from the interface. Through this time, an integration window for (3.9) cannot be defined that does not also include the shock; thus $h(t)$ is undetermined near $t = 0$.

The initial post-shock perturbation amplitude $h(0^+)$, required for comparison to the analytic models of the instability, is given by the estimate due to Meshkov (1969),

Parameters	$h(0^+)$ by (3.10)	Simulation $h(0^+)$
$M_I = 1.05,\ A = 0.2$	0.930350	0.930343
$M_I = 1.05,\ A = 0.6$	0.948345	0.948290
$M_I = 1.21,\ A = 0.2$	0.762441	0.762353
$M_I = 1.21,\ A = 0.6$	0.823618	0.823527
$M_I = 2.20,\ A = 0.2$	0.402234	0.402303
$M_I = 2.20,\ A = 0.6$	0.548190	0.548037

TABLE 4. Comparison of estimates for $h(0^+)$ obtained from $k = 0$ simulations and the approximation (3.10). To three or four significant figures, the measures are identical.

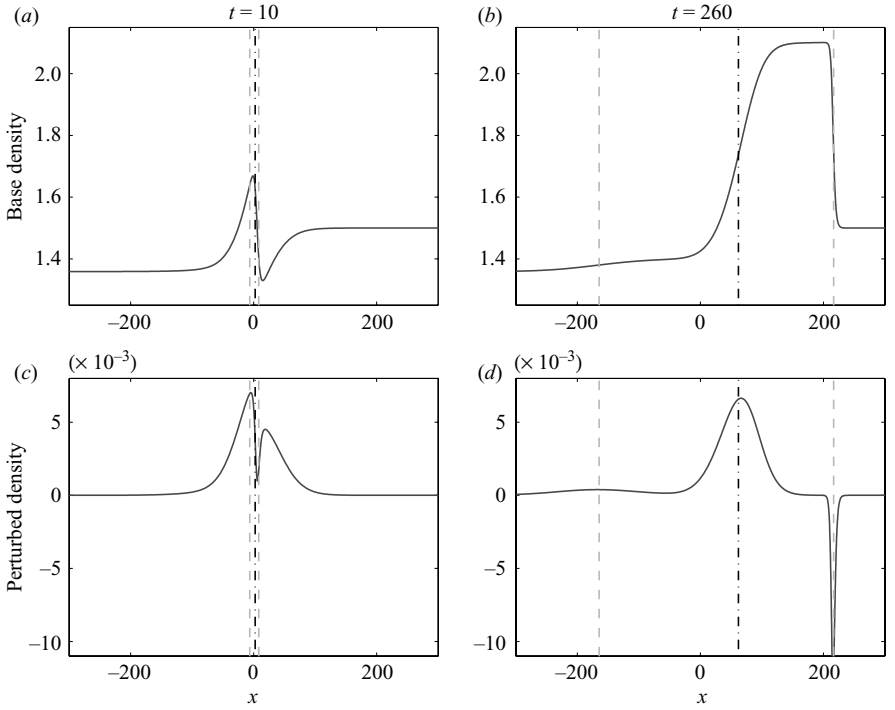

FIGURE 3. Demonstration of the ambiguity during the shock-interface interaction: (*a*, *c*) solution at a time during interaction, where interface and shock are indistinguishable; (*b*, *d*) at later time, where interface and shocks have separated. The base flow density solution is shown in (*a*, *b*) and the first-order perturbation in (*c*, *d*). The Euler interface location is indicated by the dot-dashed line, and shock locations by the dashed lines.

which models the compression of the perturbation by the incident shock:

$$h(0^+) = \left(1 - \frac{\Delta U}{U_I}\right) h(0^-). \tag{3.10}$$

Agreement of this measure with that obtained from simulations with $k = 0$ is shown in table 4. These simulations have finite ρ' and therefore a measurable amplitude $h(t)$, but physically represent a planar 'perturbation' of the interface that has no instability, the numerical equivalent to the null experiments of Collins & Jacobs (2002). The use of the estimate (3.10) avoids the problem of the shock/interface ambiguity at early times.

4. Models of the instability

4.1. *Impulsive model*

The simplest model for the RM instability, proposed originally by Richtmyer (1960), approximates the problem by an impulsively accelerated perturbed interface of zero thickness between two inviscid and incompressible fluids. If the interface is assumed to have small amplitude, the velocity perturbations in each fluid are also small and the problem may be linearized. From this model, the familiar linear growth in time prediction for the interface perturbation amplitude is obtained:

$$h(t) = h(0^+)\left[1 + A^+ \Delta U k t\right], \tag{4.1}$$

where $h(0^+)$ is the initial post-shock amplitude of the perturbation (taking into account compression of the interface by the shock), ΔU is the post-shock speed of the interface, k is the wavenumber of the perturbation and A^+ is the post-shock Atwood number. The underlying assumptions of this model break down as the incident shock strength increases, resulting in significantly less accurate growth rate predictions in these cases (Yang *et al.* 1994; Wouchuk & Nishihara 1997).

The post-linear regime is beyond the scope of this study, but nonlinear models do exist (e.g. Zhang & Sohn 1997; Herrmann *et al.* 2008), and experimental evidence points to the growth becoming nonlinear at late times (Collins & Jacobs 2002; Jacobs & Krivets 2005). At this point, the interface has transitioned from sinusoidal through the appearance of 'bubbles and spikes' to the onset of turbulence. In this work, the focus is on the start-up and early-time linear behaviour of the interface perturbation.

4.2. *Viscous model corrections*

Viscous effects on the RM instability are often ignored, with the few exceptions of models by Mikaelian (1993) and Carlès & Popinet (2001), and some recent simulations (e.g. Yee & Sjögreen 2007). In each case, viscosity damps the growth of the instability, though the models disagree strongly as to the extent of the attenuation. The models of Mikaelian (1993) and Carlès & Popinet (2001) begin with a linearization of the incompressible viscous NS equations, but use different approaches to solve the resulting equations. The Mikaelian model assumes the same x-velocity profile in each fluid as the impulsive model, thus ignoring any contribution from viscosity in the x direction, while Carlès and Popinet approximate viscous effects at the interface using a boundary layer-type approximation with matched asymptotic expansions to extend the solution to the outer inviscid region. Carlès and Popinet demonstrate that their model is superior to that of Mikaelian, which is verified in the present results.

The model of Carlès & Popinet (2001) gives the amplitude estimate

$$h(t) = h(0)\left[(1 + A\Delta U k t) - \frac{16}{3\sqrt{\pi}} \frac{\sqrt{\rho_2\mu_2}\sqrt{\rho_3\mu_3}}{(\rho_2 + \rho_3)(\sqrt{\rho_2\mu_2} + \sqrt{\rho_3\mu_3})} A\Delta U k^2 t^{3/2}\right], \tag{4.2}$$

where an additional higher order term of the second mode (e^{2iky}) has been neglected, since this cannot be expressed in the present first-order formulation unless it is extended to second order. The neglected term is of order k^3t^2; vanishingly small in the cases considered here. Following the impulsive model, the initial amplitude $h(0)$ and Atwood number A are taken as the post-shock values.

4.3. *Characteristic start-up time*

In Lombardini (2008), a modified version of the impulsive theory is used to characterize the start-up process of the RM instability, leaving the asymptotic growth

rate $\dot{h}_\infty$ as a parameter of the model. The key extension of this model is the imposition of moving plane boundaries at the trailing edges of each shock, recognizing that in the early growth phase of the instability, the proximity of the reflected and transmitted shocks will trap waves in the interface region and alter the initial growth rate. At later times, the effect of these finite boundaries diminishes as the shocks move further away, and so the model approaches the infinite-boundary state of the impulsive theory.

The key result is a characteristic time scale τ, during which the proximity of the shocks strongly influences the interface growth rate. This is defined by

$$\tau = \frac{1}{2k}\left(\frac{1-A^+}{-(U_R-u_2)} + \frac{1+A^+}{U_T-u_3}\right), \tag{4.3}$$

where A^+ is the post-shock Atwood number, U_R is the reflected shock speed, U_T is the transmitted shock speed and $u_2 = u_3 = \Delta U$ is the speed of the interface. Note that $(U_R - u_2) < 0$ and $(U_T - u_3) > 0$ are the shock speeds in the post-impact frame in which the interface is stationary for $t > 0$. For time $t \gg \tau$, the linear asymptotic growth rate is recovered.

4.4. *Asymptotic linear theory*

Detailed comparison of our linearized NS simulation results will be made to the model of Wouchuk (2001). This is an inviscid model that uses a truncated series expansion of the linearized RM problem, and captures the main physical phenomena driving the instability: the initial deposition of vorticity on the interface by the incident shock, bulk vorticity generated behind the reflected and transmitted shocks, and reverberation of sound waves between the shock fronts. This model has been shown to accurately predict asymptotic growth rates for intermediate-strength shocks in the inviscid approximation or in shock-capturing NS simulations (Wouchuk 2001; Herrmann *et al.* 2008; Lombardini 2008).

From Wouchuk & Nishihara (1997), the asymptotic growth rate of the perturbation amplitude is given exactly (in the linear theory) by

$$\dot{h}_\infty = \frac{-\rho_3 v_3(0^+) + \rho_2 v_2(0^+)}{\rho_3 + \rho_2} + \frac{\rho_3 F_3 + \rho_2 F_2}{\rho_3 + \rho_2}, \tag{4.4}$$

where the state numbering follows figure 1, and $v_2(0^+)$ and $v_3(0^+)$ are the tangential velocities at the interface (in the limiting sense of $x \to 0$) in each fluid immediately after impact. The functions F_2 and F_3 are central to the improved prediction of this model, as they represent the sonic interactions between the shocks and the interface. These functions have not been calculated analytically, so are approximated by a truncated series expression.

For weak shocks, the first term of (4.4) is dominant, the model giving results similar to the impulsive model (4.1). The second term becomes more important as shock strength increases (or for highly compressible fluids), adding a correction for the vorticity generated by the shocks upon impact. Table 5 compares predictions of asymptotic growth rate $\dot{h}_\infty / kh(0^-)$ from (4.1) and (4.4) for each of the parameter cases considered. Also shown is the start-up time scale τ, scaled by wavenumber, defined by (4.3).

Incident shock M_I	1.05	1.05	1.21	1.21	2.20	2.20
Pre-shock A	0.2	0.6	0.2	0.6	0.2	0.6
Post-shock A^+	0.19999	0.59998	0.1996	0.5991	0.1839	0.5597
Impulsive model $\dot{h}_\infty$	0.01295	0.02934	0.03616	0.08703	0.04421	0.1386
Wouchuk model $\dot{h}_\infty$	0.01341	0.03010	0.04058	0.09303	0.06030	0.1556
$k\tau$ from (4.3)	1.2137	1.9612	1.4688	2.4826	2.8224	4.9086

TABLE 5. Predictions for the asymptotic growth rate $\dot{h}_\infty/kh(0^-)$, using the impulsive model and Wouchuk (2001) model, and the characteristic start-up time proposed by Lombardini (2008), for the cases presented in this work in dimensionless form. The start-up time $k\tau$ is normalized by the scale $1/U_I$.

5. Results

5.1. *Approaching the inviscid limit*

To characterize the viscous RM problem, relevant length scales are identified as the incident shock thickness Δ_I, the interface thickness Δ_C, the interface wavelength $\lambda = 2\pi/k$, and the mean free path in the state 0 fluid $\ell_0 = \nu/\tilde{a}$, where ν is the averaged kinematic viscosity $\nu = (\mu_2 + \mu_3)/(\rho_2 + \rho_3)$, and $\tilde{a}$ is the characteristic sound speed defined by (2.4). Note that $\Delta_I \sim \ell_0$, and is a known function of the incident shock Mach number. The interface thickness Δ_C is a parameter of the initial condition.

A Reynolds number at the interface is defined (in terms of dimensional quantities) by

$$Re_I \equiv \frac{\Delta U \lambda}{\nu}, \tag{5.1}$$

where ΔU is the interface velocity. It is expected that as Re_I increases, the inviscid limit is approached and the simulation results should approach the predictions of the inviscid models. Equation (5.1) can be expressed in non-dimensional form in terms of the wavenumber k, using the same length scale ℓ_0 as before, according to

$$Re_I = \left(\frac{\Delta U}{\tilde{a}}\right)\frac{2\pi}{k}. \tag{5.2}$$

The term of (5.2) in parentheses is determined by the initial conditions of the incident shock, while the second term is a free parameter of the simulation and controlled by the choice of k for a given initial condition. The dimensionless length scales

$$\eta \equiv k\Delta_C \quad \text{and} \quad \zeta \equiv \Delta_C/\Delta_I$$

specify the relative initial diffusiveness of the interface and the thickness of the interface relative to the shock. To approach the inviscid limit of $Re_I \to \infty$, a sequence of simulations is performed with decreasing k and increasing Δ_C such that η is held constant (but small). This necessarily implies that ζ increases with Re_I in each sequence. This is a subtly different distinguished limit from that encountered with discontinuous interface treatments, where $\Delta_C \to 0$ is implicit, but the exploration of the parameter space shown in the following sections does yield information on both limits. Note also that the growth and start-up time scale (4.3) of the instability scales strongly with k, increasing with Re_I the simulation time required to reach the linear growth phase.

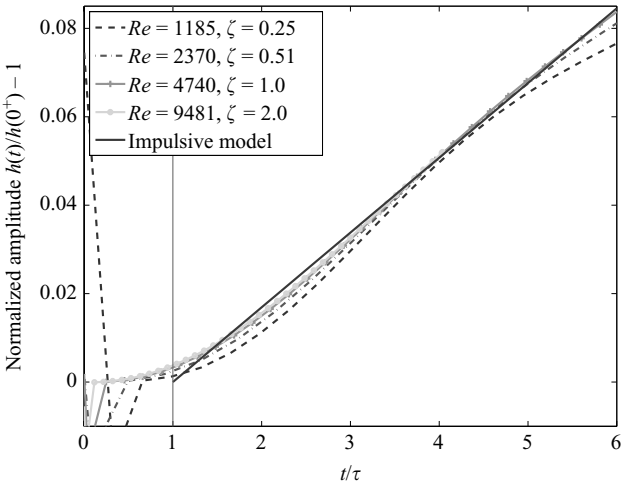

FIGURE 4. Plots of normalized perturbation amplitude $h(t)/h(0^+) - 1$ against time scaled by the start-up time τ from Lombardini (2008), with comparison to the impulsive model growth, for the case $M_I = 1.05$, $A = 0.2$, across a range of Reynolds numbers.

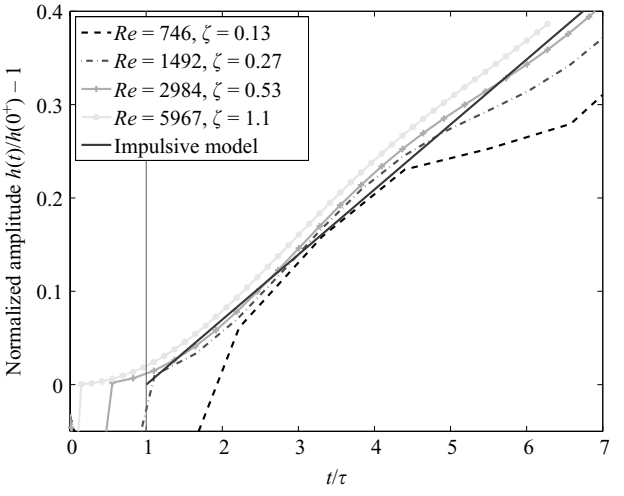

FIGURE 5. Similar plots to figure 4, this for the case $M_I = 1.21$, $A = 0.2$. See § 5.4 for further discussion of the case $Re_I = 746$, where viscosity has a significant effect.

5.2. *Start-up phase*

We begin presentation of the simulation results with examination of the start-up time scale proposed by Lombardini (2008) and defined in (4.3). Figures 4–6 show plots of perturbation amplitude $(h(t)/h(0^+) - 1)$ against time scaled by τ for a range of Reynolds numbers. These show collapse of the growth profiles in the inviscid limit, demonstrating a time scaling for the instability on kt. At lower Reynolds numbers, deviation from the analytic models is evident, but towards the inviscid limit, growth follows the impulsive model prediction closely for $t > \tau$ in the weak to intermediate shock strength examples. In the strong shock case, growth follows instead the asymptotic model prediction of Wouchuk (2001).

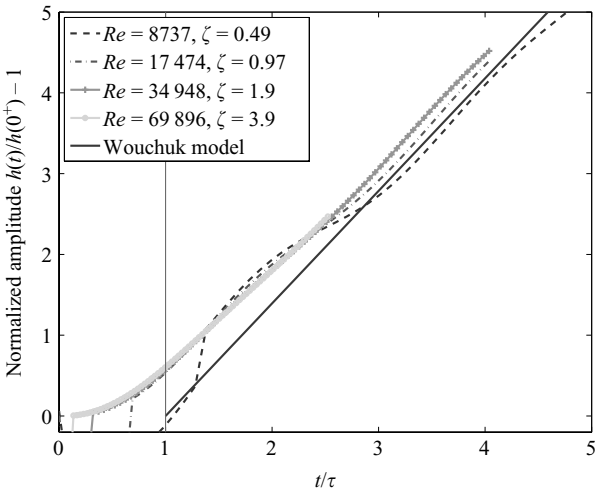

FIGURE 6. Similar plots to figure 4, this for the case $M_I = 2.20$, $A = 0.6$. Comparison here is to the asymptotic model growth of Wouchuk (2001).

Based on figures 4 and 5, a simple model for amplitude growth rate that accounts for start-up of the instability is proposed:

$$\frac{\dot{h}(t)}{h(0^+)} = \begin{cases} 0, & t \leqslant \tau, \\ A^+ \Delta U k, & t > \tau. \end{cases} \tag{5.3}$$

This has the form of a shifted time origin for the impulsive model, and appears to closely approximate the simulated growth profiles in the inviscid limit. For stronger shocks, the impulsive model growth rate assumption may be inappropriate: compare figure 6, where the model of Wouchuk (2001) is substituted instead. In this case also the linear regime appears to be reached in a time somewhat less than τ. Note that for most physical problems, the start-up time scale is very small; here $\tau \sim 10^{-7}$ s.

5.3. *Analytic model comparisons*

A more precise comparison between the simulation results and analytic models is made by examining the growth rate of the instability. Shown in figures 7–9 are the growth rates of the interface perturbation, scaled by wavenumber, for a range of cases. Both the impulsive model and that of Wouchuk (2001) predict that growth rate under this scaling should approach a constant value in the inviscid limit. The simulation results show this trend. Oscillation observed in the amplitude growth rate is qualitatively similar to that observed by, among others, Yang *et al.* (1994); Wouchuk (2001); Herrmann *et al.* (2008). The amplitude of this oscillation decreases strongly with increasing Reynolds number, indicating that the oscillatory effect is amplified by viscous effects, across all incident shock strengths. The frequency of oscillation is found to be weakly dependent on Reynolds number.

Evidence that the inviscid limit is properly approached in figures 7–9 by the method outlined in § 5.1 is given by figure 10. This shows amplitude growth rates, scaled by wavenumber, for a range of similar Reynolds numbers and two values for the interface wavelength to thickness ratio η. The similarity of scaled growth rates (at comparable Reynolds numbers) for different η indicates that the same limit is approached independently of η as the shock becomes thin relative to the interface.

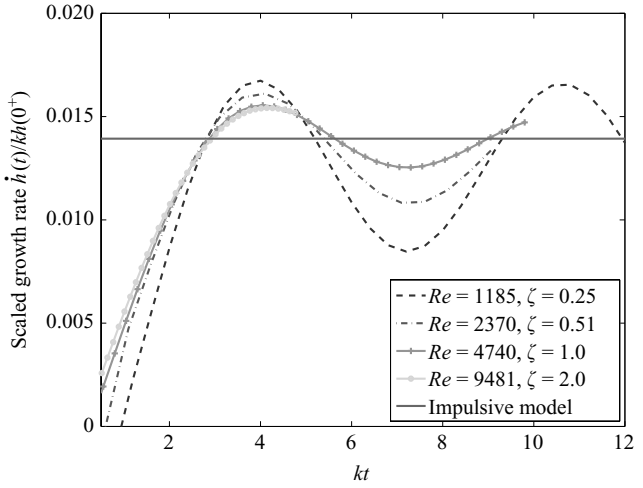

FIGURE 7. Plots of perturbation amplitude growth rate $\dot{h}(t)/kh(0^+)$ against dimensionless scaled time kt, for the case $M_I = 1.05$, $A = 0.2$ with varying Reynolds number. Comparison is to the asymptotic growth rate predicted by the impulsive model (4.1).

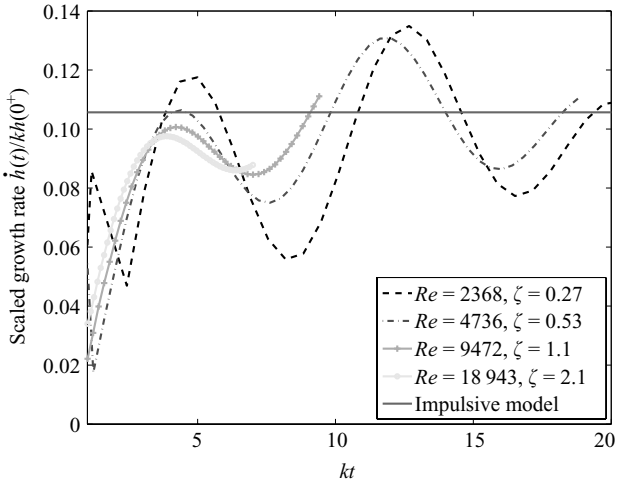

FIGURE 8. Similar growth rate plots to figure 7, for the case $M_I = 1.21$, $A = 0.6$. Comparison is to the asymptotic growth rate predicted by the impulsive model (4.1).

Figures 11–13 focus on a particular Reynolds number simulation for each of three cases: a weak shock $M_I = 1.05$ with $A = 0.6$, an intermediate shock $M_I = 1.21$ with $A = 0.6$, and a strong shock $M_I = 2.20$ and $A = 0.2$. Amplitude growth rates $\dot{h}(t)/h(0^+)$ are compared to the time evolution model of Wouchuk (2001). Wave numbers quoted are non-dimensional values.

In the weak shock case, figure 11 confirms that the impulsive model is a good approximation of the asymptotic growth rate of the instability under these conditions. The average scaled growth rate from the simulation, after the initial transient, is 1.244×10^{-5}, compared to 1.240×10^{-5} for the impulsive model prediction. The simulation growth rate evolution generally agrees well with the Wouchuk (2001) model, sharing many features of the time history. Asymptotically, however, the

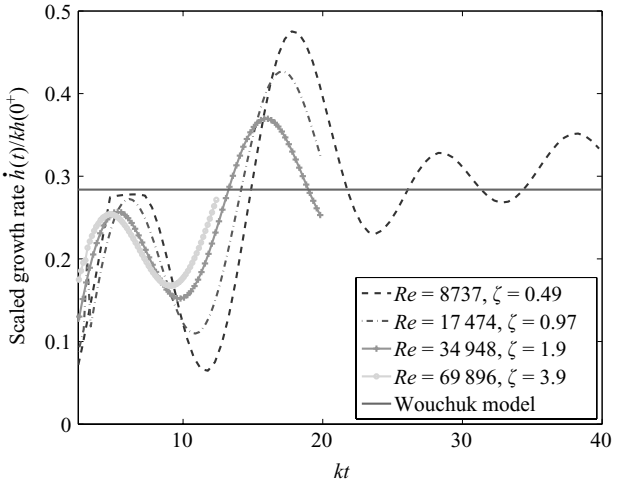

FIGURE 9. Similar growth rate plots to figure 7, for the case $M_I = 2.20$, $A = 0.6$. Comparison is to the asymptotic growth rate prediction from Wouchuk (2001).

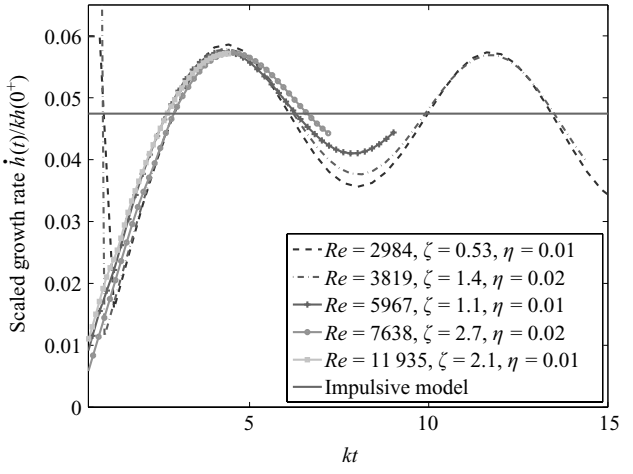

FIGURE 10. Plots of perturbation amplitude growth rate $\dot{h}(t)/kh(0^+)$ against dimensionless scaled time kt, for the case $M_I = 1.21$, $A = 0.2$. Both Reynolds number and interface wavelength to thickness ratio η vary in this case.

simulation tracks a little lower than the model; it is possible that this is due to a small attenuating viscous effect present at this Reynolds number.

The intermediate case shown in figure 12 has similar parameters to the experiments of Collins & Jacobs (2002): $M_I = 1.21$ and $A = 0.6$. The simulation results show that long-term growth rate is centred closely on the impulsive model prediction, a conclusion supported by the good agreement shown by this model in figures 8 and 12 for all but the lowest Reynolds number cases. Upon correcting for diffuse interface effects, the experiments of Collins & Jacobs (2002) come to a similar conclusion (for the linear regime). In this case, the model of Wouchuk (2001) appears to slightly overestimate the asymptotic growth rate. It is notable also that the model underpredicts the amplitude of the first peak in the growth rate calculated from the simulation, for both this case and $M_I = 1.05$. Further, after this peak, there appears

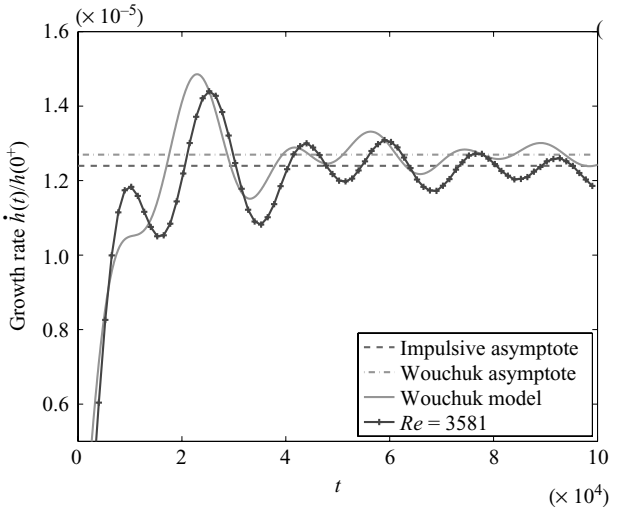

FIGURE 11. Plot of non-dimensional amplitude growth rate $\dot{h}(t)/h(0^+)$, for $M_I = 1.05$, $A = 0.6$ and physical wavenumber $k = 6018$ m^{-1}, with asymptotic growth rate predictions shown for impulsive and Wouchuk (2001) models. Overlaid also is the time history predicted by Wouchuk's theory.

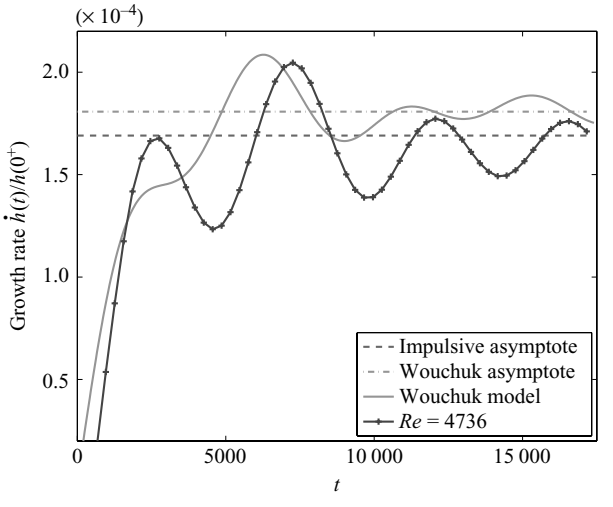

FIGURE 12. Plot of non-dimensional amplitude growth rate $\dot{h}(t)/h(0^+)$, for $M_I = 1.21$, $A = 0.6$, and physical wavenumber $k = 24070$ m^{-1}, with asymptotic growth rate predictions shown for impulsive and Wouchuk (2001) models. Overlaid also is the time history predicted by Wouchuk's theory.

to be a phase difference between our results and the model, which we speculate may be due to very early start-up effects detected only by full resolution of the shock and interface, as in the present study.

Some evidence for this theory may come from Herrmann *et al.* (2008) (cf. figure 4 in particular). This compares the result of a two-dimensional NS simulation of the instability at $M_I = 1.21$ (at a Reynolds number in the inviscid range) with Wouchuk's model, to excellent agreement. Their simulation uses a shock capturing/tracking

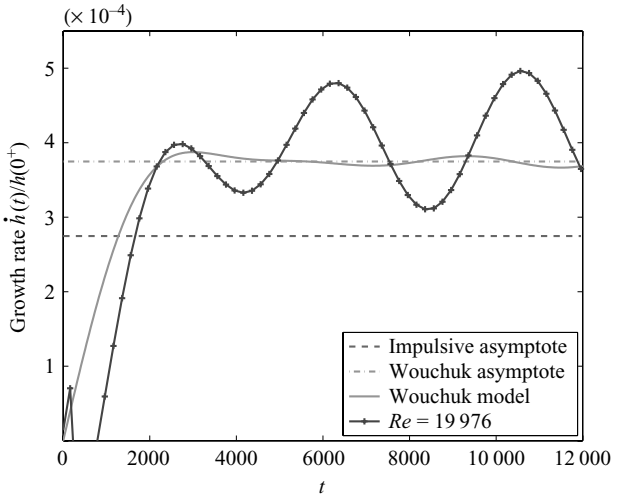

FIGURE 13. Plot of non-dimensional amplitude growth rate $\dot{h}(t)/h(0^+)$, for $M_I = 2.20$, $A = 0.2$ and physical wavenumber $k = 37610$ m^{-1}, with asymptotic growth rate predictions shown for impulsive and Wouchuk (2001) models. Overlaid also is the time history predicted by Wouchuk's theory.

method and treats the interface as a level set scalar, so it is discontinuous for all time. This implies that the fundamental assumptions of the Herrmann *et al.* simulations are more similar to Wouchuk's inviscid model than these results at the early growth stages of the instability; neither can capture the early time effects observed in the present simulations.

In the strong shock case, the simulation results point unambiguously to Wouchuk's model being the best estimate of the asymptotic growth rate. Figures 9 and 13 confirm this, with the plot of growth rate showing oscillation about the Wouchuk prediction. However, comparison of the time histories in figure 13 shows that the model considerably underpredicts the magnitude of oscillation in the growth rate. This implies that the amount of acoustic energy trapped between the shocks in the interface region is underestimated by the model, caused by the difficulty involved in calculating the contribution from the transmitted shock by the truncated series method. The present simulation results confirm that this is a significant effect under these conditions: integrating to compare the amplitude predictions indicates that although early-time agreement is good, the effect of the oscillations in growth rate contribute to an overprediction of the amplitude by the model at later times.

5.4. *Influence of viscosity*

Based on the present results, we can conclude that contact with the inviscid limit has been made. The primary Reynolds number effect that is observed is simply due to the dependence of Re_I on the wavenumber k; this is confirmed by the majority of results and the collapse of amplitude histories when the effect of k has been scaled out. In the cases where viscous effects are seen, attenuation of the growth rate is observed when compared to the inviscid models.

Figures 14 and 15 show some particular examples where viscous effects are significant. For the case $Re_I = 239$ in figure 14, viscous attenuation is large enough to cause decay of the interface perturbation, suppressing the instability. The model of Carlès & Popinet (2001) predicts that decay occurs in this case, but overestimates

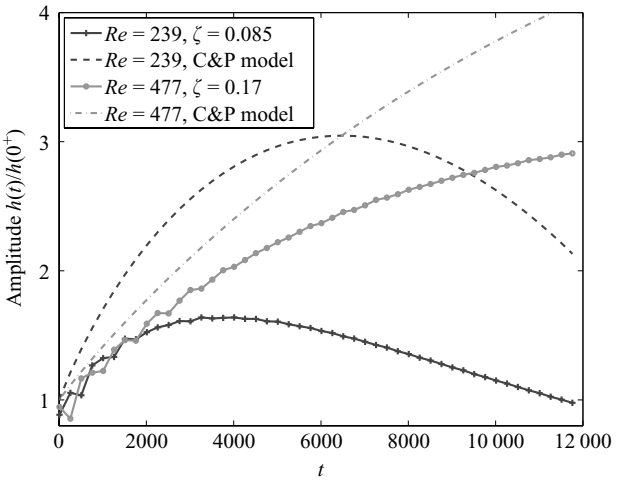

FIGURE 14. Plots of non-dimensional perturbation amplitude for $M_I = 1.21$ and $\eta = 0.02$, for low Reynolds numbers. Dashed lines show the predictions of the Carlès & Popinet (2001) model for each case. At low enough Re_I, viscous effects are sufficient to cause decay of the perturbation.

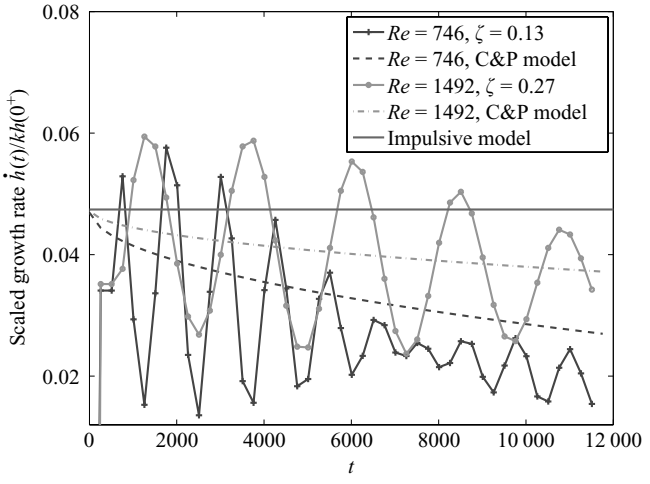

FIGURE 15. Plots of non-dimensional perturbation amplitude growth rate $\dot{h}(t)/kh(0^+)$ against scaled time kt for $M_I = 1.21$, for low-Re_I cases affected by viscosity. Comparisons are made to the growth rate predictions of the Carlès & Popinet (2001) model and the impulsive model.

the maximum amplitude and the time scale of the decay. Figure 15 compares growth rates from the present simulations with the Carlès and Popinet model for low Reynolds numbers. In this case, the decay envelope is captured with reasonable accuracy, particularly for $Re_I = 1492$ where the oscillation in the growth rate is closely centred on the model prediction. Note that the model cannot be expected to capture oscillations in the growth rate as no attempt is made to estimate effects caused by proximity of the shocks.

Comparison of viscosity-influenced cases from the present results suggests some bounds on the Reynolds numbers at which viscous effects are significant. Based on the present simulations, for $Re_I < 1000$, viscosity has a significant attenuating

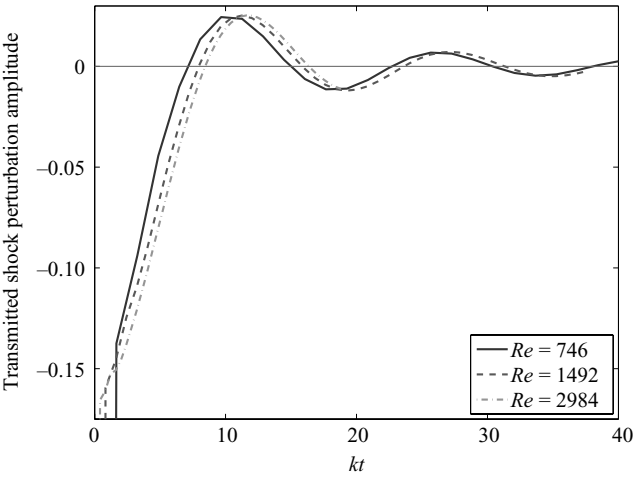

FIGURE 16. Transmitted shock perturbation amplitude plotted against dimensionless scaled time kt, for the case of $M_I = 1.21$ and $A = 0.2$, showing collapse of the curves across Reynolds number.

influence on the amplitude growth rate. In the range $1000 < Re_I < 5000$, there may be a small viscous effect, but attenuation is small enough that the inviscid models are an acceptable approximation. Beyond this, the asymptotic behaviour of the interface amplitude is essentially indistinguishable from the inviscid approximation. This is in qualitative agreement with Yee & Sjögreen (2007).

5.5. *Shock perturbations*

Upon interaction with the interface perturbation, the reflected and transmitted shocks develop perturbations of their own. These perturbations are stable (Landau & Lifshitz 1959; Erpenbeck 1962), unlike the interface perturbation, and are expected to decay with time. This is confirmed by the simulation results, which show that the perturbation amplitude oscillates within a decaying envelope at both the reflected and transmitted shocks. Also notable is that the amplitude perturbation passes through zero multiple times as it decays, and that the reflected shock amplitude is initially of opposite sign to the transmitted shock amplitude.

The collapse of the interface perturbation amplitude curves when plotted against time scaled by the perturbation wavenumber (kt) suggests that a similar scaling may apply to the shock perturbations. For the transmitted shock perturbation, this is generally true, illustrated by the example in figure 16, where collapse is very good except at the lowest Reynolds number cases. On the other hand, the reflected shock perturbation does not appear to collapse similarly when plotted against kt (figure 17). The spatial frequency of the reflected shock perturbation is necessarily k by the form of the linearization, and the reason for a different time frequency dependence for the reflected shock is unclear.

6. Conclusions

The start-up and linear growth phases of the RM instability have been investigated using a novel high-order shock-resolved NS simulation. By assuming a linearized form for the solution with a perturbed interface, where the base flow is the solution to the nonlinear one-dimensional NS equations for a shock incident on a density

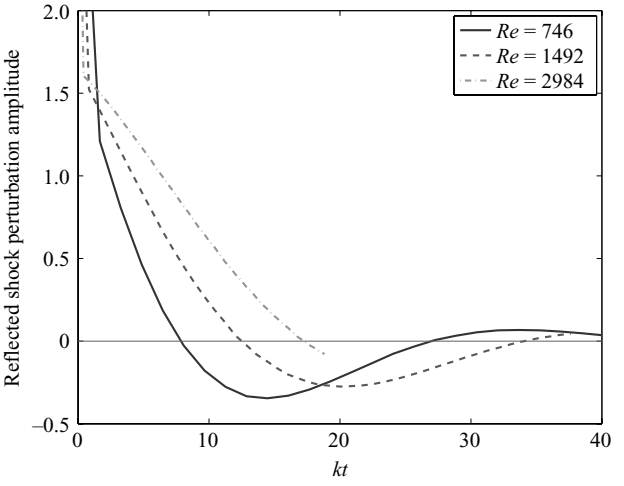

FIGURE 17. Reflected shock perturbation amplitude plotted against dimensionless scaled time kt, for the case $M_I = 1.21$ and $A = 0.2$, showing that similar collapse does not occur with this scaling.

interface, the problem could be reduced to a spatially one-dimensional configuration. To efficiently resolve the full internal structure of the shocks, the high-order grid interface closures of Kramer *et al.* (2007) were employed in a refinement scheme that tracked the solution features based on the inviscid Riemann solution. This numerical method ensures that observed viscous effects are caused only by physical viscosity.

Results from the simulations show that for weak and intermediate strength shocks, the impulsive model is adequate for prediction of the asymptotic growth rate of the perturbation. For strong shocks, the model from Wouchuk (2001) accurately predicts the asymptotic growth rate. The characteristic start-up time proposed by Lombardini (2008) is verified as a good estimate of the time for the instability to enter the linear growth regime. Transient growth shows general agreement with Wouchuk's model for weaker shocks, though some new features are observed, while for stronger shocks the same model significantly underestimates the amplitude of oscillation in the growth rate. The extent of the influence of viscosity is predicted by a Reynolds number based on the perturbation wavenumber. Existing models of viscous attenuation are found to unreliably predict the growth rate of the instability in most cases.

This work was supported by the ASC programme of the Department of Energy under subcontract number B341492 of DOE contract W-7405-ENG-48. The authors would like to thank Gustavo Wouchuk for his valuable assistance for providing details of his model.

REFERENCES

BROUILLETTE, M. & STURTEVANT, B. 1994 Experiments on the Richtmyer–Meshkov instability: single-scale perturbations on a continuous interface. *J. Fluid Mech.* **263**, 271–292.

BUTCHER, J. C. 2003 *Numerical Methods for Ordinary Differential Equations*. Wiley.

CARLÈS, P. & POPINET, S. 2001 Viscous nonlinear theory of Richtmyer–Meshkov instability. *Phys. Fluids* **13** (7), 1833–1836.

Carpenter, M. H., Gottlieb, D. & Abarbanel, S. 1994 Time-stable boundary conditions for finite difference schemes solving hyperbolic systems: methodology and application to high-order compact schemes. *J. Comput. Phys.* **111** (2), 220–236.

Collins, B. D. & Jacobs, J. W. 2002 PLIF flow visualization and measurements of the Richtmyer–Meshkov instability of an air/SF_6 interface. *J. Fluid Mech.* **464**, 113–136.

Duff, R. E., Harlow, F. H. & Hirt, C. W. 1962 Effects of diffusion on interface instability between gases. *Phys. Fluids* **5** (4), 417–425.

Engquist, B. & Sjögreen, B. 1998 The convergence rate of finite difference schemes in the presence of shocks. *SIAM J. Numer. Anal.* **35** (6), 2464–2485.

Erpenbeck, J. J. 1962 Stability of step shocks. *Phys. Fluids* **5** (10), 1181–1187.

Fornberg, B. 1988 Generation of finite-difference formulas on arbitrarily spaced grids. *Math. Comput.* **51**, 699–706.

Herrmann, M., Moin, P. & Abarzhi, S. I. 2008 Nonlinear evolution of the Richtmyer–Meshkov instability. *J. Fluid Mech.* **612**, 311–338.

Hill, D. J., Pantano, C. & Pullin, D. I. 2006 Large-eddy simulation and multiscale modelling of a Richtmyer–Meshkov instability with reshock. *J. Fluid Mech.* **557**, 29–61.

Jacobs, J. W. & Krivets, V. V. 2005 Experiments on the late-time development of single-mode Richtmyer–Meshkov instability. *Phys. Fluids* **17**, 034105.

Jones, M. A. & Jacobs, J. W. 1997 A membraneless experiment for the study of Richtmyer–Meshkov instability of a shock-accelerated gas interface. *Phys. Fluids* **9** (10), 3078–3085.

Kramer, R. M. J. 2009 Stable high-order finite-difference interface schemes with application to the Richtmyer–Meshkov instability. PhD thesis, California Institute of Technology, Pasadena.

Kramer, R. M. J., Pantano, C. & Pullin, D. I. 2007 A class of energy stable, high-order finite-difference interface schemes suitable for adaptive mesh refinement of hyperbolic problems. *J. Comput. Phys.* **226**, 1458–1484.

Landau, L. D. & Lifshitz, E. M. 1959 *Fluid Mechanics*. Pergamon.

Lombardini, M. 2008 Richtmyer–Meshkov instability in converging geometries. PhD thesis, California Institute of Technology, Pasadena.

Meshkov, E. E. 1969 Instability of the interface of two gases accelerated by a shock wave. *Sov. Fluid Dyn.* **4** (5), 151–157.

Mikaelian, K. O. 1991 Density gradient stabilization of the Richtmyer–Meshkov instability. *Phys. Fluids* A **3** (11), 2638–2643.

Mikaelian, K. O. 1993 Effect of viscosity on Rayliegh–Taylor and Richtmyer–Meshkov instabilities. *Phys. Rev.* E **47**, 375–383.

Richtmyer, R. D. 1960 Taylor instability in shock acceleration of compressible fluids. *Commun. Pure Appl. Math.* **13**, 297–319.

Saffman, P. G. & Meiron, D. I. 1989 Kinetic energy generated by the incompressible Richtmyer–Meshkov instability in a continuously stratified fluid. *Phys. Fluids* A **1** (11), 1767–1771.

Svärd, M., Carpenter, M. H. & Nordström, J. 2007 A stable high-order finite difference scheme for the compressible Navier–Stokes equations, far-field boundary conditions. *J. Comput. Phys.* **225**, 1020–1038.

Whitham, G. B. 1974 *Linear and Nonlinear Waves*. Wiley.

Wouchuk, J. G. 2001 Growth rate of the linear Richtmyer–Meshkov instability when a shock is reflected. *Phys. Rev.* E **63** (5), 056303.

Wouchuk, J. G. & Nishihara, K. 1997 Asymptotic growth in the linear Richtmyer–Meshkov instability. *Phys. Plasmas* **4** (4), 1028–1038.

Yang, Y., Zhang, Q. & Sharp, D. H. 1994 Small amplitude theory of Richtmyer–Meshkov instability. *Phys. Fluids* **6** (5), 1856–1873.

Yee, H. C. & Sjögreen, B. 2007 Simulation of Richtmyer–Meshkov instability by sixth-order filter methods. *Shock Waves* **17**, 185–193.

Zhang, Q. & Sohn, S. 1997 Nonlinear theory of unstable fluid mixing driven by shock wave. *Phys. Fluids* **9** (4), 1106–1124.